Journal of Alloys and Compounds 804 (2019) 494–502

Contents lists available at ScienceDirect

Journal of Alloys and Compounds

journal homepage: http://www.elsevier.com/locate/jalcom

# Novel method for construction of high performance nanocrystalline FeCuNbSiB toroidal core

Taylan Günes

*Department of Energy Systems Engineering, Yalova University, 77100, Yalova, Turkey*

ARTICLE INFO

*Article history:*
Received 30 April 2019
Received in revised form
2 July 2019
Accepted 3 July 2019
Available online 4 July 2019

*Keywords:*
Nanocrystalline alloy
Stress annealing
Stress induced winding system
Structural deformation

ABSTRACT

In the current study magnetic, magneto-optical and microstructural properties of the amorphous $Fe_{83}Cu_1Nb_3Si_5B_8$ alloy were properly investigated depending on the external treatments such as annealing and stress annealing. Kinetic nanocrystallization temperatures of certain ribbon were determined at the range of 500–510 °C. The amorphous ribbons produced in the as-spun state were subjected to tensile stress loading with and without rapid heat treatment of 510 °C during 5 s. Behaviors of certain ribbons were extensively investigated in terms of several factors such as magnetic properties, microstructural evaluation, magneto-optical effects and structural deformation by means of quasi-static hysteresis loops, XRD analyses, TEM micrographs, magneto-optical Kerr imaging and nanoindentation test. Present nanocrystalline $Fe_{83}Cu_1Nb_3Si_5B_8$ alloy have allowed yielding not only ultrafine grain structure of around 7.02 nm but also saturation induction of 1.85 T, coercivity of 5.8 $A.m^{-1}$ and saturation magnetostriction of 6 ppm. Additionally, based upon determined optimum stress annealing circumstances, toroidal nanocrystalline core was produced using a proposed *stress induced winding (SIW) system.* SIW system based principally on the gradient of the rotational speed of each mandrel in the standard toroidal core winding machine. Structural deformation of the core was determined by an analysis method performed on the ribbon. Accordingly, induced elastic modulus ($E$), Poisson's ratio ($\mathbb{V}$) and residual strain ($\varepsilon$) in the ribbon under the influence of stress annealing by 200 MPa at 510 °C were found as 7.9 GPa, 0.39 and 0.031, respectively.

© 2019 Elsevier B.V. All rights reserved.

## 1. Introduction

Over the last decades, nanocrystalline (NC) FeCuNbSiB soft magnetic materials produced as-spun (AS) state from amorphous precursor by the primary crystallization of bcc Fe have attracted much attention as they have superior magnetic properties [1–3]. NC FeCuNbSiB alloys are commonly known by lowest coercivity, $H_c$ (<1 A/m), fulfilling permeability, $\mu$ ($>1 \times 10^5$) with quite low magnetostriction, $\lambda_s$ (<1 ppm) and sufficient saturation polarization, $J_s$ ($\approx$1.9 T) [1–4] as long as DC magnetic field is applied. Such produced ribbons have been widely investigated in terms of both magnetic properties [1,5–7] and microstructures [8–12]. Hoffman et al. [10] and Gonzalez et al. [13] investigated magnetic behaviors of NC soft magnetic ribbon after proper annealing conditions were implemented under tensile stress, i.e., stress annealing. Alves et al. [14] showed that stress annealing requires a continuous reel-to-reel annealing technique with possibly short annealing times. Here the point determines the standard for the control of stress inducing during reel-to-reel production process. Expectation from a stress annealed sample obtains superior magnetic capabilities after such short time annealing treatments lasting a few seconds only [15]. On the other hand, sustainable structural stability should be consistently assured for the long-term usage. Lashgari et al. [16] showed that annealing treatment increased the hardness and *Young's modulus* of FeSiB alloys, while further increase of the annealing time (i.e. 500 °C–3 h) led to decreasing hardness and *Young's modulus.* Thus, the stability and durability of the sample were more or less reduced with the stress annealing as long time for heat treatment causes to increase of brittleness of the ribbon.

The objective of the present work is to summarize the influence of rapid heating and rapid heating under the tensile loading on the magnetic properties, microstructural evaluations and structural deformation of FeCuNbSiB alloy. Jiang [17] stated that depending on the changes in the annealing duration, the magnitude of the grain sizes in NC alloys could fluctuate as a result of the variations in the nucleation and volume diffusion rates. This fluctuation makes the

*E-mail address:* taylan.gunes@yalova.edu.tr.

https://doi.org/10.1016/j.jallcom.2019.07.031
0925-8388/© 2019 Elsevier B.V. All rights reserved.

ribbon unstable and brittle even in small external interferes as well. The main case is herein to control the applied tensile stress during reel-to-reel production process by means of proposed SIW system. This process makes possible to manage the value of desired stress. Then the produced toroidal core could be exposed to either thermal treatment only or annealing with the presence of the magnetic field. In particular, heat treatment in the presence of magnetic field in which the direction can be transverse, longitudinal or perpendicular depending on the desired magnetic properties lead to the formation of the less complex domain configuration [18,19]. On the other hand, after production of the toroidal core, the most remarkable parameter that affects to the magnetic properties is the real-time value of the tensile loading. Since winding-induced bending stress has also been activated during core production, the tolerance comparison between linear (before core production) and non-linear (after core production) tensile stress implementations must be investigated. Regardless of unstable winding, in other word, release the wound core as “loose”, improvement in saturation magnetization leads to reduce in core loss.

Ribbons, analyzed by a sequence of microstructural analyses after produce, were used to manufacture the toroidal core in the last stage. In the case of core production, a winding machine which has binary or ternary equivalent mandrels is generally preferred to control the wall thickness of the core. However, in the course of fabrication of the core, a numerical expression which determines the desired stress loading is so far missing. During this extensive study, we have aimed to put forward a numerical explanation to control the stress during the core production. Also, this numerical expression which is principally derived from the fundamental stress/strain equations and depends on the difference between the rotational speeds of mandrels was properly input the system's algorithm. Moreover, physical variations in the ribbons such as longitudinal ($\varepsilon_L$) and transversal ($\varepsilon_T$) strains, Young's modulus ($E$) and Poisson's ratio ($\mathbb{V}$) could be determined by means of nanoindentation test.

## 2. Experimental section

Precursor amorphous ribbons with the nominal composition of $Fe_{83}Cu_1Nb_3Si_5B_8$ were prepared by induction melting under a high-purity argon atmosphere. The thickness of produced as-spun ribbon was found ~20 μm. It was quantitatively confirmed by both scanning electron microscope (SEM) micrograph and electronic caliper. The material was slit to 20 mm width. The annealing was performed by continuously transporting the ribbon through a furnace with an approximately 10 cm long homogeneous temperature zone under a tensile stress $\sigma$, along the ribbon axis during 5 s. Note that the sample was subjected to stress implementation as long as annealing was performed. The alloys in the AS state were isothermally evaluated by differential scanning calorimetry (DSC) at a heating rate of 0.67 °C/s under continuous heating and a nitrogen flow. Accordingly, primary crystallization temperatures (first-peak) were obtained around 510 °C. The microstructures of the ribbons both in the AS state and in the states of annealed and stress annealed were characterized by X-ray diffraction (XRD) by using monochromated Mo-Kα radiation ($\lambda = 7.1\ nm$). Coercivity ($H_c$), was determined from the DC hysteresis loops recorded on 0.3 m long ribbon samples. The saturation induction ($B_s$) was determined from the hysteresis loop at a maximum field strength of 20 kA/m. The saturation magnetostriction ($\lambda_s$) was measured by the small angle magnetization rotation (SAMR) method [20]. The grain size was determined by the Scherrer equation using a form factor $K = 0.9$. However, numerous limitations should also be considered since the correlation between D and $H_c$ is necessary to ensure the reliability of actual calculation [21]. Mean grain size was further analyzed using transmission electron microscope (TEM) with an accelerating voltage of 200 kV. TEM samples were prepared onto the plate with the diameter of 3 mm by ion milling method (Gatan Inc., PIPS-M695) under liquid nitrogen cooling condition. The magnetization process of the samples was confirmed both by simultaneous hysteresis measurements and by domain observation. The sample was magnetized in a specially designed single-sheet frame magnet [22]. The magnetized coil was driven by a Kepco power supply. For domain observation, Kerr microscope was preferred; a regular wide-field polarization microscope that allows for high-resolution imaging using the longitudinal Kerr effect with adjustable sensitivity direction [23]. To perform the nanoindentation test, surface of the sample was polished down to a final grit of 40 nm. Nanoindentation was performed using a TriboIndenter (TI 950, Hysitron Inc., USA). The indenter tip in the form of triangular pyramid is made of an industrial diamond with an elastic modulus of 120 GPa and Poisson's ratio of 0.12. While the tip had a triangle geometry with the angle of 142.3°, it was truncated at a height of 2 μm and its radius was assigned as 100 nm. In this study, we used the quasistatic nanoindentation module to measure the Young's modulus and related mechanical properties.

## 3. Results & discussion

### 3.1. Magnetic, microstructural and magneto-optical investigations

Quasi-static hysteresis loops resulting from progressively applied tensile stresses in the range of 10–200 MPa are indicated in Fig. 1a. Here the ribbons in the as-spun state were merely exposed to the tensile loading regardless of heat treatment. Thereby their magnetic behaviors illustrates that the longitudinal tensile stress lead to formation of soft magnetic materials to ensure the higher saturation induction. However, it is apparently seen that $H_c$ values was increased as well as $B_s$ values. Thus, increase in the $B_s$ value allows good magnetic capability while expanded area of hysteresis curve (increasing $H_c$) means enlarged grain size. This case indicates that the improvement in magnetic properties is not sustainable by means of only stress loading. Nevertheless, this unstable state could be annihilated considering a mild heat treatment in addition to the tensile stress, namely stress annealing. In the Fig. 1b, the curves became much uniform where $B_s$ value increased while $H_c$ became relatively less than before. Note that in the second case (Fig. 1b), ribbons were annealed at 510 °C in the presence of tensile loading in the range of 10–200 MPa just like the case in Fig. 1a. Appropriate temperature of heat treatment could be assigned by means of DSC analysis results are shown in Fig. 2a.

According to DSC analysis as shown in Fig. 2a, kinetic primary crystallization temperatures of $Fe_{83}Cu_1Nb_3Si_5B_8$ alloy system were found at about 510 °C. Then, the ribbon in the states of AS, stress loaded, annealed and stress annealed was individually compared by XRD studies (Fig. 2b). Herewith, it can be explicitly seen the evolvement of the diffraction patterns during the nanocrystallization process from the state of AS to stress annealing. This broadened reflections denotes the formation of large volume fractions DO3-type ordered nanocrystals of α-Fe(Si) solid solution.

The new formations after only mechanical (stress), only thermal and thermal under the influence of magneto-mechanical treatments are evidence of the *decreased grain size*. The intensity of diffraction peak may lead to predict the crystallization volume fraction of certain nanocrystalline alloy with respect to its counterparts [24]. Note that all XRD analyses were performed in the free surface of the ribbons. According to intensity peaks of the ribbon in the AS state, crystallization was more or less formed towards free-surface even if amorphous matrix was still dominant. This structure shows that in-plane crystalline-texture was formed during casting

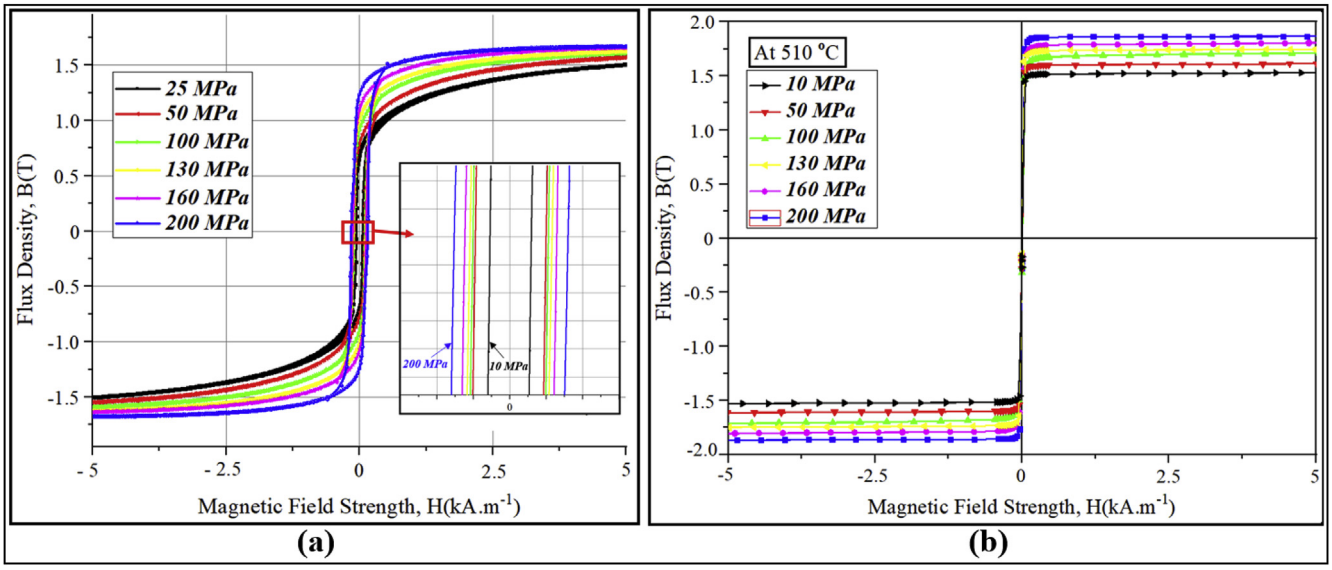


**Fig. 1.** Effect of tensile loading in the $Fe_{83}Cu_1Nb_3Si_5B_8$ alloy system. Ascending full hysteresis curves of the ribbon in the as-spun state (a) and variation of $H_c$ values (inset). Ascending full hysteresis curves after application of stress annealing from 10 to 200 MPa (b).

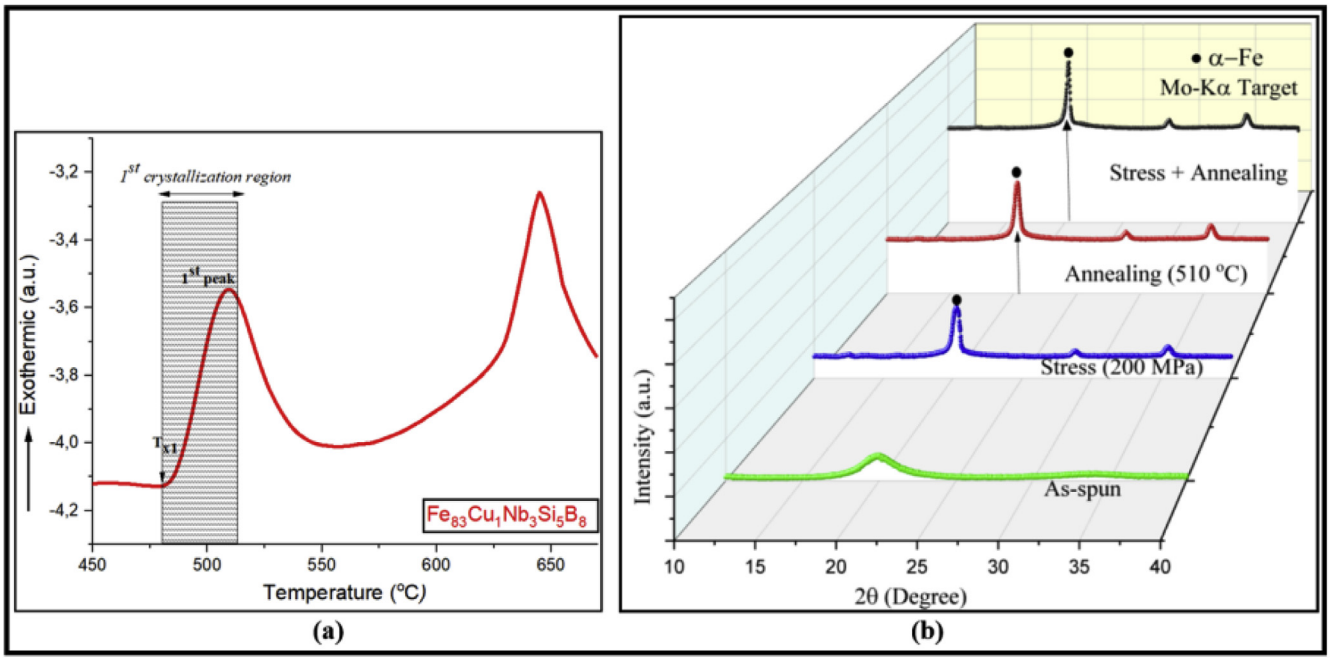


**Fig. 2.** Typical DSC curve for composition of $Fe_{83}Cu_1Nb_3Si_5B_8$ alloy system (a) and 3D X-ray diffraction patterns of the ribbons in the AS state, after apply tensile stress of 200 MPa, annealing at 510 °C and stress annealing during 5 s (b). Mo-Kα source was preferred as radiation.

in the direction of wheel rotation. Such physical variations of the diffraction peaks mean the reduction in the crystal grain size that can be easily calculated by Scherrer formula,

$$D = \frac{k\lambda}{\beta Cos\theta} \quad (1)$$

where $D$ denotes average crystalline size, $\beta$ is the line broadening in radians that is known as full width of half maximum (FWHM), $\theta$ is the Bragg angle and $\lambda$ represents X-ray wavelength (For Mo-Kα target). Using FWHM of the diffraction peak of the α-Fe(Si) crystalline phase and the Scherrer equation, the calculated $D$-values of the alloys after the implementation of mechanical stress, annealing and stress annealing were found at 25.1 nm, 8.1 nm and 5.7 nm with the nominal errors of ±1.2, ±0.24 and ± 0.082, respectively. This calculation is generally based on the random anisotropy model developed by Herzer [25]. However, in some cases, the obtained or calculated $D$ values should be quantitatively proven by TEM imaging and the statistical distribution of the average grain sizes.

TEM micrographs shown in Fig. 3a–c is the remarkable evidence to become ultrafine grain sizes applying stress annealing during 5 s. The choice of five seconds as the duration of the heat treatment is to avoid reducing the stability of the sample. Apparently, flash annealing performed within 5 s would bring a smart solution for

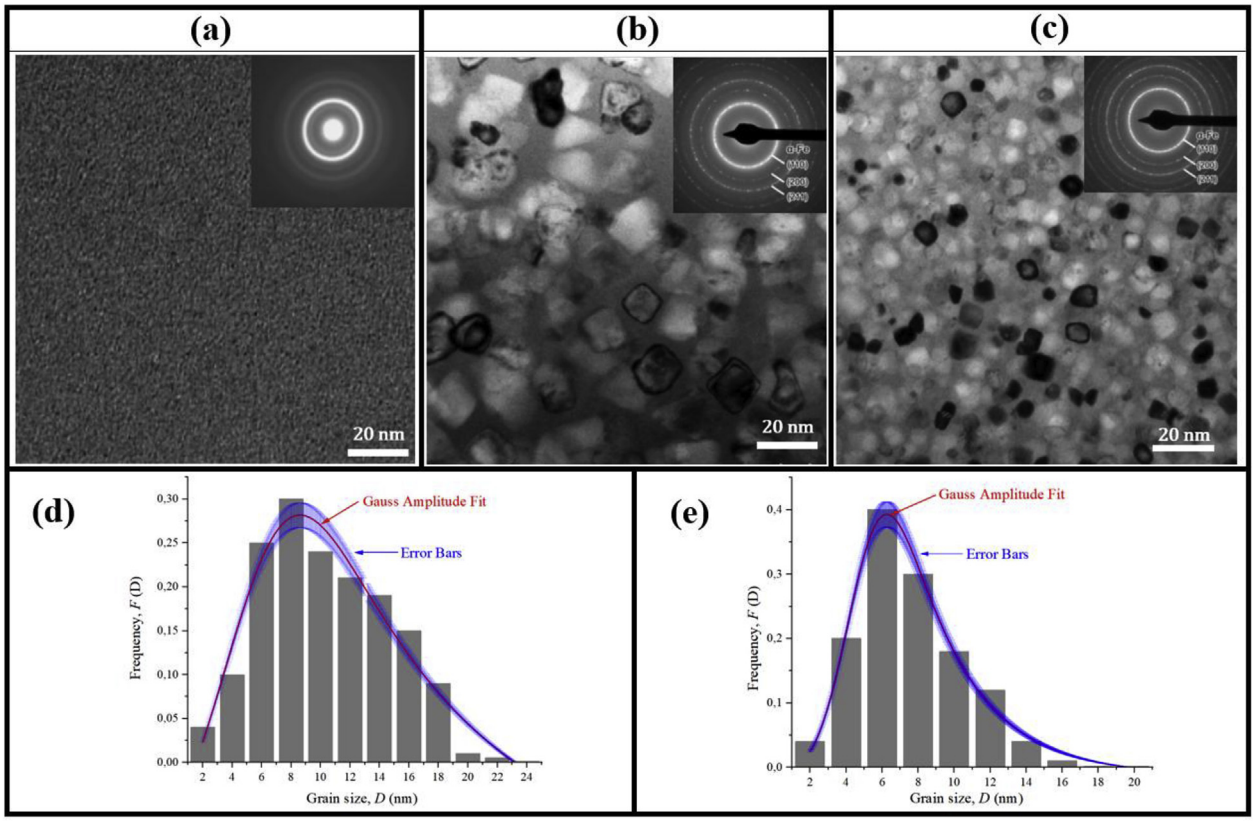


**Fig. 3.** TEM micrographs for the specimen in the AS-state (a), in the state of heat treatment by 510 °C (b) and stress annealing at 200 MPa (c). Besides, the statistical distribution of the average grain sizes for (b) and (c) were illustrated in (d) and (e), respectively.

this problem. In Fig. 3a, the specimen in the AS state shows a few signs of crystallization on the free surface while the sample exposed to heat treatment in Fig. 3b obviously consists of relatively bigger grains (in the vicinity of 6–15 nm). The specimens subjected to stress annealing indicate subsequently small average grain sizes ranging from 4 to 10 nm as shown in Fig. 3c. A statistical grain size distributions for the samples after a mild heat treatment and stress annealing are also presented with frequency distribution and its Gauss Amplitude fitting. The average grain sizes from statistical distributions were found around 6.14 nm (for stress annealed sample) and 8.99 nm (for the sample subjected to heat treatment) which have a good correlation with the data yielded by XRD. Thus, deviation between calculated mean grain sizes by TEM and XRD analyses were found by 5% for stress annealed sample and by 22% for the sample exposed to heat treatment only. It is noted that such difference between two cases probably originates from the random anisotropy of the sample exposed to annealing without stress loading that sustains more or less its existence.

Fig. 4 shows the variations of saturation induction of $B_s$, saturation magnetostriction of $\lambda_s$, coercivity of $H_c$ and mean grain size ($D$) as a function of tensile stress loading under the influence of heat treatment at 510 °C. Variations of $B_s$ and $H_c$ could be principally predictable from the comparison between Fig. 1a and b which lead to inverse ratio between them. Note that this study was performed under the constant temperature which is around the first crystallization region. Due to this fact, stress loading is mere factor to affect the microstructural evaluation of the ribbons. Particularly, $D$-values show a remarkable reduction trend after the stress loading between 100 MPa and 200 MPa. This peculiar result leads to formation of less boride structure and of small crystalline grain sizes around such values of external loadings. Additionally, reduction trend of $\lambda_s$ is also quite similar with $H_c$ that shows preferably linear reduction with the increment of stress loading. Thus stress annealing under higher values of stress loading has a dominant effect for the improvement of microstructural properties, i.e. $D$, $\lambda_s$ and $B_s$.

In Fig. 5, magneto-optical Kerr micrographs are presented to exhibit the refinement in magnetic microstructures depending on the circumstances of tensile loading without a mild heat treatment. The stress patterns in the AS state (Fig. 5a) can particularly appear to be superimposed onto a regular wide domain structure. The observations of such characteristic internal stress patterns are to be expected unless the specimen is subjected to the external thermal and/or mechanical treatments. It should be noted that presented image sequences in Fig. 5 were observed on the sample of AS state (a) and on the samples exposed to tensile stresses in the range of 10–200 MPa (b-g). Regardless of the effect of magnetic field, it is clear that applied tensile stress vitiates somewhat residual stress patterns which can appear to be superimposed on the wide domain patterns where curved domains are along the principal direction. Therefore, the annihilation of certain stress patterns was not permanently enhanced without implementation of tensile force in the presence heat treatment. In this sense, comparison between annealed and stress annealed samples under the same circumstances is illustrated as shown in Fig. 6. Here the tensile force with a mild heat treatment was activated until the physical integrity of the ribbon was lost (>200 MPa) and expectedly, strong enough tensile force led to form slab-like domains along the planar tensile axis as the prevailing magnetization process (Fig. 6b).

On the other hand, sample exposed to rapid heat treatment at 510 °C during 5 s shows less uniform domain configuration (Fig. 6a) than that of annealed sample. Therefore, stress annealing makes

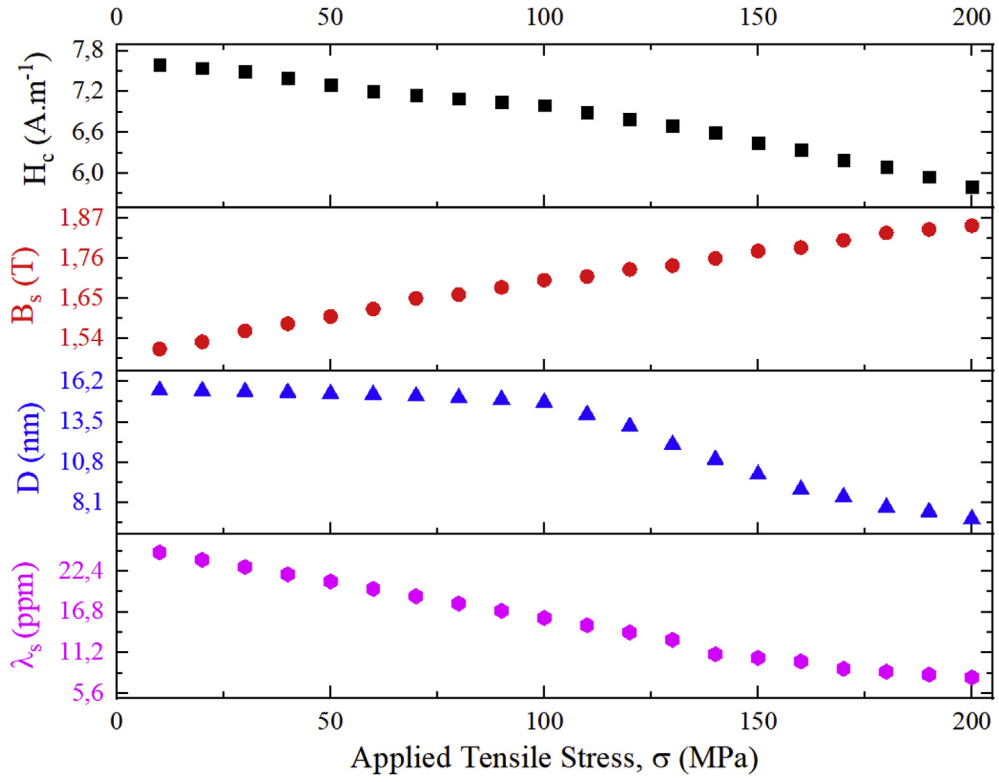


**Fig. 4.** Variations of coercivity $H_c$, saturation induction $B_s$, mean grain size $D$ and saturation magnetostriction $\lambda_s$ as a function of tensile stress loading under the influence of heat treatment at 510 °C.

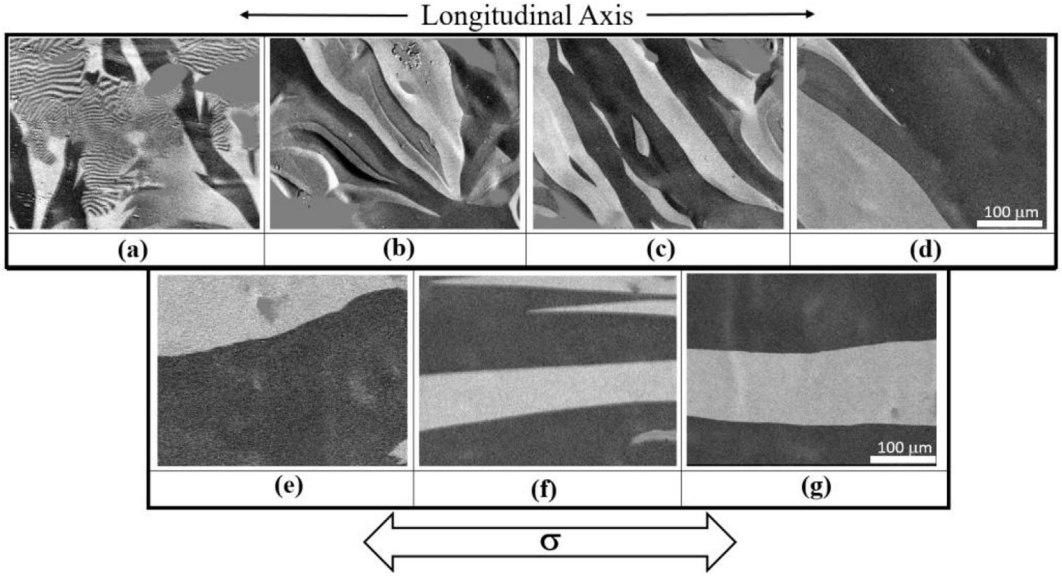


**Fig. 5.** Magneto-optical Kerr micrograph; stress domination patterns in the as-quenched state (a), tensile stressed pattern of 10 MPa (b), 50 MPa (c), 100 MPa (d), 130 MPa (e), 160 MPa (f) and 200 MPa (g).

possible to obtain uniform domain arrangement with less curved walls. This case may also lead to the inhomogeneous magnetization in which it appears fluctuating magnetization direction due to the existence of the average random magnetocrystalline anisotropy [26].

### 3.2. Structural deformation during core production

In the second part of this investigation, we aimed to bring reasonable solution to produce the toroidal core with the containable values of applied tensile stresses in the lab conditions.

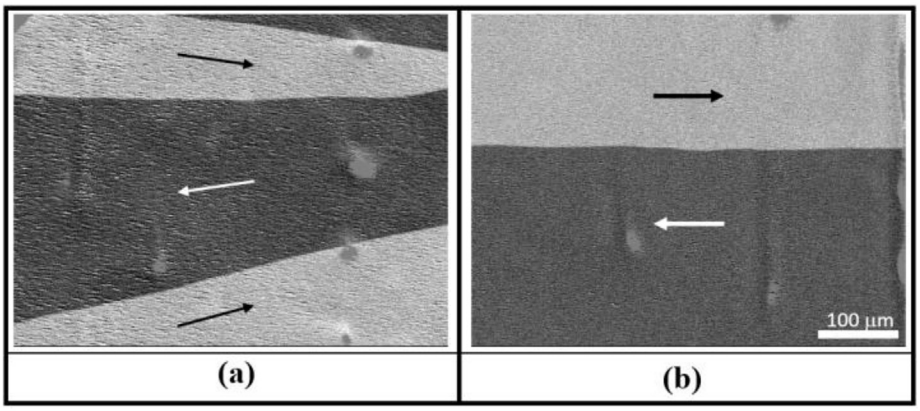


**Fig. 6.** The domain evaluation based on nanocrystallization of the sample by means of annealing at 510 °C (a) and of stress annealing at 510 °C and 200 MPa (b).

To meet this requirement, we proposed a formula which is based on the stress and strain relations. Thereby, nanocrystalline toroidal core was able to be produced by means of a standard winding machine with and without stress loading. Ribbons were also analyzed to ensure the structural deformation using nano-indentation test device. As it is well-known that volume fractions of the grain interior and the grain boundary exchange during grain size is expanded [27], produce the core in the presence or absence of the stress loading becomes significant in terms of nanocrystallization.

As common-known that the tensile force $(F)$ applied to the sample in a cross-sectional area $(A)$ could be expressed by $F/A$ which is the definition of tensile stress loading $(\sigma = F/A)$. Combination of this relation with the Newton's second law $\left(F = m.\frac{dv}{dt}\right)$ leads to new formation of the formula that includes the term of the linear velocity, as indicated in Eq. (2),

$$\sigma(v) = \frac{m}{A_o - A_N}\,\frac{d}{dt}(v_1 - v_2) \tag{2}$$

where $A_o$ and $A_N$ represents original and subsequent cross-sectional areas, respectively. As one can be established that there is close relation between the terms of “stress” and “strain”. This numerical relation can be validated for the winding machines that have a binary mandrel systems. Thus, mandrels having different linear velocities providing that $v_1 > v_2$ lead to form a stress during core production. So, deformation inside the sample by applied external stress can be defined as “strain” or “residual strain” and expressed as in Eq. (3),

$$\varepsilon = \frac{L_N - L_o}{L_o} \tag{3}$$

where $L_o$ and $L_N$ represents original and subsequent length of the ribbons, respectively, while $\varepsilon$ defines the strain value. In this sense, Young's modulus can be written by combination of (2) and (3) as in Eq. (4),

$$E = \frac{\sigma}{\varepsilon} = \frac{1}{r}\,\frac{m.L_o}{(A_o - A_N)(L_N - L_o)}\,\frac{d}{dt}(\omega_1 - \omega_2) \tag{4}$$

where $\omega_1$ and $\omega_2$ define the angular speed of each mandrel. Here the term of $r$ refers to the radius of the holder attached to the mandrel. It is here given to cancel out the term of $r$ placed in the numerator resulting of relation between linear and angular speeds $(v_n = \omega_n.r)$, where the subscript $n$ varies with the number of stacked ribbon in each holder. Schematically illustration of the proposed *stress induced winding (SIW) system* is given in Fig. 7. Physical parameters of a piece of ribbon was also configured as long as the tensile stress was induced by rotation of the mandrels as shown in Fig. 7a. The proposed system that includes binary mandrels seems a simple machine just like a tape recorder (Fig. 7b). The mandrel, known as “Source” has a tunable resistive force in which it acts like attempting a reverse motion with respect to pulling velocity. This behavior allows to change of applied tensile stress as well as residual strain during the construction of toroidal core. Here the point is the gradient of the rotational speed of each mandrel, $\omega_1$ and $\omega_2$.

The proposed formula, namely *stacking function* as presented in Eq. (5) was applied to the mandrels of the winding machine to obtain desired stress values. Thus, it was formed a difference between the rotational speeds of source and target mandrels where they rotate to a counter-clockwise.

$$\boldsymbol{D(\sigma,\ \omega) = \frac{(A_o - A_N)}{m.r}\ n(\sigma)\int_0^n \sigma(t)\,dt} \tag{5}$$

where $D(\sigma, \omega)$ represents stacking function depending upon applied tensile stress and the rotational speed of the mandrels. One of the most significant parameters in the stacking function is the stacking or winding number, $n(\sigma)$ as a function of applied tensile stress, because the thickness of the produced core progressively varies with the time. Due to this fact, subscript, $n$ was introduced once the linear velocity $(v_n)$ was replaced with the angular speed $(\omega_n)$. Boundary of the definite integral in (5) denotes the increase of the wall thickness of the core as a function of the time.

The wall thickness of the produced core was assigned by 30 mm. However, the number of stacked ribbons in unit volume varies with the applied tensile stress, as the air gaps between the ribbons could be reduced as much as possible. This may be interpreted that SIW system was not only offered temporarily solution to improve magnetic properties, but also provide structural stability for the produced core. Schematic illustrations of produced core under the influence of certain stress values in SIW system is given in Fig. 8. $R$ and $r$ represent the inner and outer radius of the core, $D$ and $d$ represent the wall thickness of the core and width of the ribbons. Also, $l$ defines the length of the magnetic flux path. The values of $r$, $d$, $D$, $R$ and $l$ were measured as 20 mm, 20 mm, 30 mm, 50 mm and 185 mm, respectively. As seen in the Fig. 7a, physical parameters of the ribbon such as length, width and thickness entirely vary with the applied stress where the ribbon stretches from original length

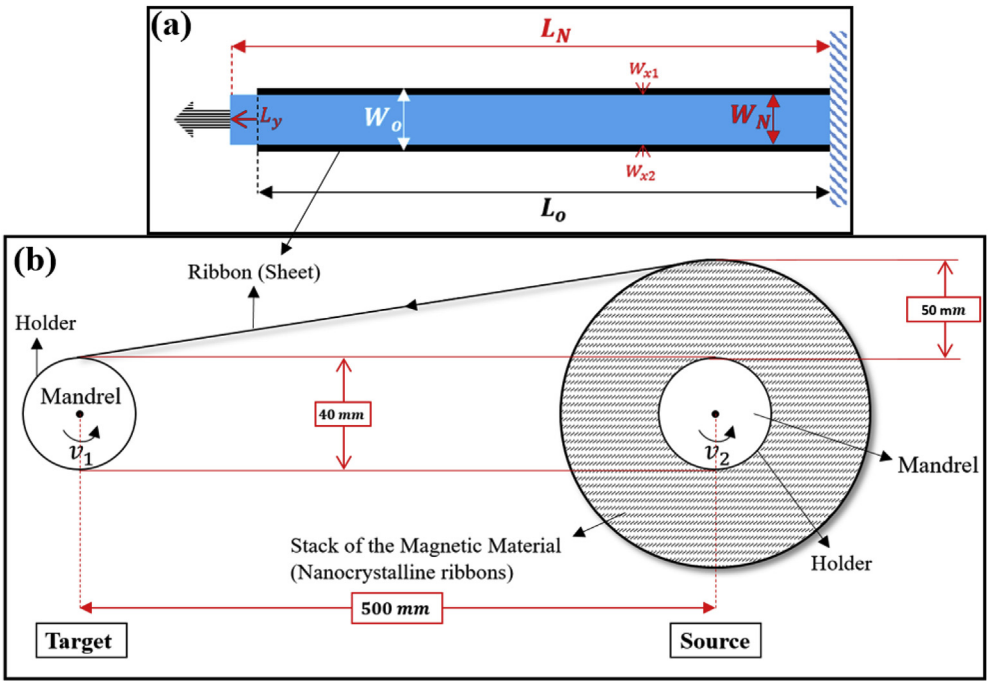


**Fig. 7.** Sketch of the proposed SIW system. Physical evaluation after applied tensile stress to a piece of the ribbon (a). Construction procedure of toroidal core depending on pulling velocity (b).

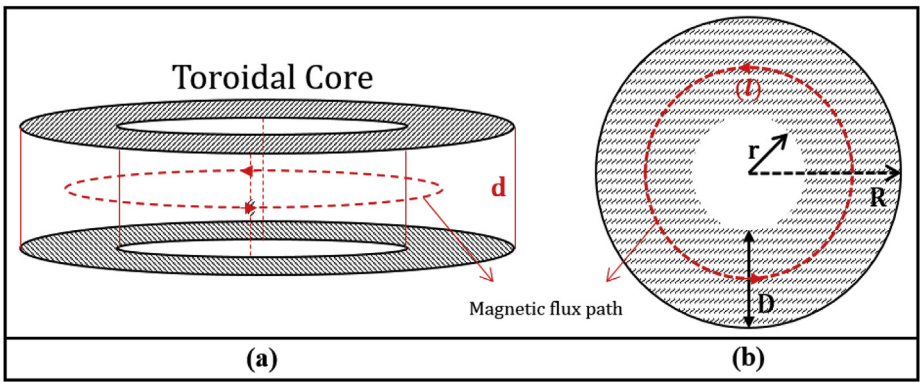


**Fig. 8.** Produced core dimensions. Appearance from the side view (a) and the top view (b).

($L_o$) or width ($W_o$) to new length ($L_N$) or width ($W_N$). Thus cross-sectional area is simultaneously decreased depending on strength of the applied stress as well. The difference of such physical parameters could be quantitatively determined by nanoindentation test. Thereby, Eq. (6a-b) is given to reveal structural deformation during core production.

$$L_N = L_o + L_y \tag{6a}$$

$$W_N = W_o - 2W_x \tag{6b}$$

As the transversal strain ($\varepsilon_T$) and longitudinal strain ($\varepsilon_L$) could be principally identified, Poisson's ratio of the ribbon in the AS state is found by following expressions (Eqs. (7) and (8)),

$$\mathbb{V} = \frac{\varepsilon_T}{\varepsilon_L} = \left(\frac{W_N - W_o}{W_o}\right) \Big/ \left(\frac{L_N - L_o}{L_o}\right) = \frac{L_o(W_o - 2W_x - W_o)}{W_o(L_o + L_y - L_o)} \tag{7}$$

$$\mathbb{V} = \left\{\frac{-2L_oW_x)}{W_oL_y)}\right\} \tag{8}$$

where $W_x$ refers to shrinkage value in width along with the $x-$ axis, whereas $L_y$ indicates the longitudinal elongation value in $y-$ axis. In table − 1, induced stress values in the produced core depending on the gradient between the speeds of mandrels are presented. Structural deformations formed in the ribbons as a result of such tensile stress loading was determined as well. It is explicitly seen that the number of the stacked ribbons in a unit volume progressively varies with increase of tensile loading [28].

**Table 1**
Definition of structural deformation in the ribbon. Induced stress depending on the gradient speeds between mandrels, longitudinal ($\varepsilon_L$) and transversal strains ($\varepsilon_T$) with the empirical errors, Young's modulus ($E$), Poisson's ratio ($\mathbb{V}$) number of stacked ribbons in a unit volume with associated experimental errors.

| Diff. of pulling velocity $[v_2 - v_1]$ (m/sn) | Tensile Stress (MPa) | Longitudinal Residual Strain ($\varepsilon_L$) | Error (%) | Transverse Residual Strain ($\varepsilon_T$) | Error (%) | Young's Modulus (E, GPa) | Poisson's ratio ($\mathbb{V}$) | Number of stacked ribbons in unit volume (turns) | Error |
|---|---|---|---|---|---|---|---|---|---|
| ~2 | 10 | 0.0052 | ±0.9 | 0.002 | ±1.14 | 7.9 | 0.39 | 1475 | ±0.05 |
| ~10 | 50 | 0.0118 | ±1.2 | 0.0044 | ±1.27 | | | 1481 | ±0.19 |
| ~20 | 100 | 0.017 | ±1.32 | 0.007 | ±2 | | | 1485 | ±0.11 |
| ~26 | 130 | 0.021 | ±1.44 | 0.0082 | ±2.7 | | | 1488 | ±0.07 |
| ~32 | 160 | 0.0246 | ±1.51 | 0.0096 | ±2.8 | | | 1493 | ±0.22 |
| ~40 | 200 | 0.0279 | ±1.59 | 0.0109 | ±2.83 | | | 1496 | ±0.39 |

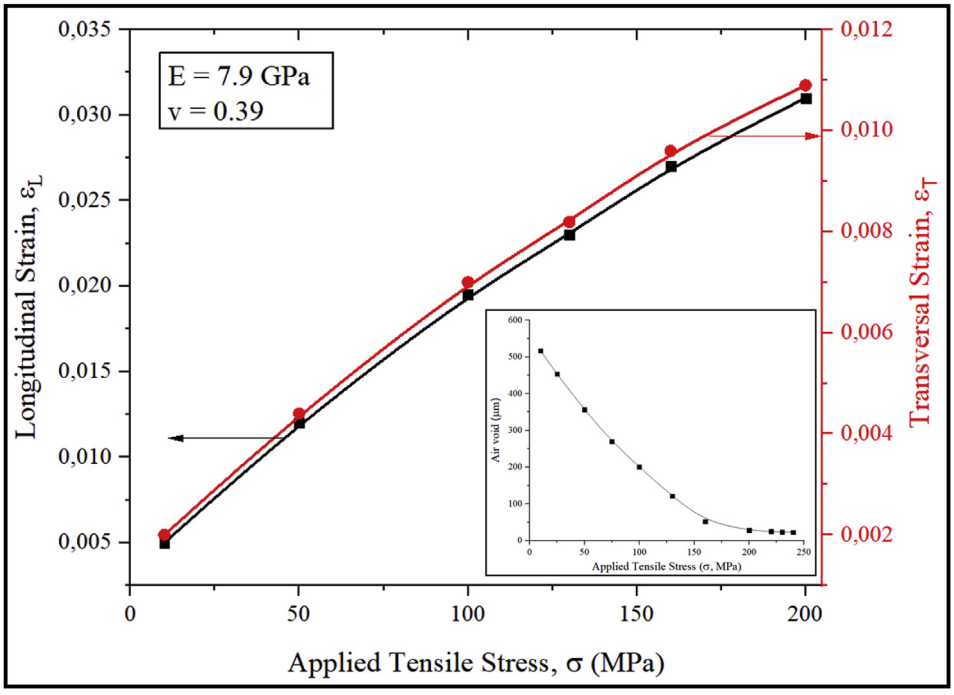


**Fig. 9.** A stress–strain diagram showing the linear elastic deformation for $\varepsilon_L$ and non-linear deformation for $\varepsilon_T$ at the constant Young's modulus ($E$) and Poisson's ratio ($\mathbb{V}$). Reduced air void between 10 and 200 MPa is showed in the inset figure.

Fig. 9 indicates the variation of $\varepsilon_L$ and $\varepsilon_T$ in the course of $x-$ and $y-$ axes, as a function of applied tensile stress loading. Herewith, we found an effective elastic modulus $E$ from the slope of a stress–strain curve [29]. As 100 mm long sample was preferred in this study, curves of $\varepsilon_L$ and $\varepsilon_T$ shows relatively different appearance. To ensure the proper value of elastic modulus $E$, $\varepsilon_L$ was approved as the reference value. Furthermore, inset graph in Fig. 9 shows the variation in the air void with the increase of tensile stress. Once the stress value is increased from 10 to 200 MPa, the number of stacked ribbons inside the toroidal core could be increased around 1.5%. Such proportion explicitly indicated that the presence of tensile stress loading contributes to both structural stability and magnetic capability of the produced toroidal NC core.

Formed air void between the stacked ribbons during construction was measured by electronic caliper. Once the wound toroidal core with no stress and fully stress loading were compared in terms of their wall thickness, it was explicitly seen that the number of ribbon increased as much as 21 layers than that of no-stress core. Accordingly, increase value of the stress loading led to form a curve in a descending trend as indicated inset graph in Fig. 9.

## 4. Conclusion

The studied alloy system involving a nanocrystalline structure and consisted of α-Fe grains with the size of 7.02 nm obtained by means of heat treatment of 510 °C under the influence of tensile stress loading as much as 200 MPa indicated low coercivity of around 5.8 $A.m^{-1}$, relatively high saturation induction of around 1.85 T and substantially low saturation magnetostriction of 6 ppm. It is quantitatively realized that the samples exposed to the stress annealing in actual circumstances have shown great magnetic capability and also superior soft magnetic properties. The average grain sizes were yielded by both TEM micrographs (statistical distribution) and XRD data (Scherrer equation) to ensure the optimum grain size distribution. It was found a difference around 8% between the data of TEM and XRD. The proposed SIW system was tested on the certain ribbons in terms of structural deformation resulting of applied tensile stress during core production. Accordingly, stress induced nanocrystalline toroidal cores in the range of 10–200 MPa were able to be produced using the gradient of the rotational speed of each mandrel. To numerically introduce the system, a relation, called as *stacking function* was brought out based on stress and

strain formulas. The concept of the stacking function is principally based on winding number $n(\sigma)$, ribbon mass ($m$), holder radius ($r$), induced stress and strain. Comparison between linear (before core production) and non-linear (after core production) tensile stress implementations showed relatively low tolerance (~1–2%). Due to this fact, the structural deformation could be estimated analyzing the ribbon by nanoindentation test device. Moreover, it was found that stress-controlled toroidal core production allows to contribute the magnetic capability as well as structural stability of the core. Based on the volume of entire core, air gaps between the stacked ribbons could be reduced around 84% after the tensile stress of 200 MPa was implemented. In addition to refinement in domain structure and annihilation of complex stress patterns, this case explicitly contributes the improvement of saturation magnetization of around 25%. On the other hand, proposed SIW system and its numerical approach contributes to develop standard auto winding machines for amorphous and nanocrystalline cores.

## Acknowledgments

This study was supported by the Research Fund of Yalova University (project number: 2017/AP/139). The author would especially like to thank the Leibniz Institute for Solid State and Materials Research Dresden (IFW) and Prof. Rudolf Schäfer for providing the opportunity to perform Kerr imaging.

## References

[1] Y. Yoshizawa, S. Oguma, K. Yamauchi, New Fe-based soft magnetic alloys composed of ultrafine grain structure, J. Appl. Phys. 64 (1988) 6044. https://doi.org/10.1063/1.342149.
[2] G. Herzer, Handbook of Magnetic Materials, first ed., Elsevier, North Holland, 1997, pp. 415–462.
[3] R. Hasegawa, Present status of amorphous soft magnetic alloys, J. Magn. Magn. Mater. 215/216 (2000) 240–245. https://doi.org/10.1016/S0304-8853(00)00126-8.
[4] R. Parsons, B. Zang, K. Onodera, H. Kishimoto, T. Shoji, A. Kato, K. Suzuki, Nanocrystallization and magnetic softening in Fe-B binary alloys induced by ultrarapid heating, J. Phys. D Appl. Phys. 51 (2018) 415001. https://doi.org/10.1088/1361-6463/aadad6.
[5] G. Herzer, Nanocrystalline soft magnetic materials, Scripta Mater. 33 (1995) 1741–1756. https://doi.org/10.1016/0304-8853(95)01126-9.
[6] A. Makino, H. Men, T. Kubota, K. Yubuta, A. Inoue, FeSiBPCu nanocrystalline soft magnetic alloys with high Bs of 1.9 Tesla produced by crystallizing heteroamorphous phase, Mater. Trans. 50 (2009) 204. https://doi.org/10.2320/matertrans.MER2008306.
[7] K. Takenaka, N. Nishiyama, A.D. Setyawan, P. Sharma, A. Makino, Performance of a prototype power transformer constructed by nanocrystalline Fe-Co-Si-B-P-Cu soft magnetic alloys, J. Appl. Phys. 117 (2015) 17D519. https://doi.org/10.1063/1.4919041.
[8] R. Schäfer, A. Hubert, G. Herzer, Domain observation on nanocrystalline material, J. Appl. Phys. 69 (1991) 5325. https://doi.org/10.1063/1.348067.
[9] G. Herzer, Creep induced magnetic anisotropy in nanocrystalline Fe-Cu-Nb-Si-B alloys, IEEE Trans. Magn. 30 (1994) 6. https://doi.org/10.1109/20.334226.
[10] B. Hofmann, H. Kronmüller, Creep induced magnetic anisotropy in nanocrystalline Fe73.5Cu1Nb3Si13.5B9, Nanostruct. Mater. 6 (1995) 961–964. https://doi.org/10.1016/0965-9773(95)00220-0.
[11] S. Flohrer, R. Schäfer, C. Polak, G. Herzer, Interplay of uniform and random anisotropy in nanocrystalline soft magnetic alloys, Acta Mater. 53 (2005) 2937–2942. https://doi.org/10.1016/j.actamat.2005.03.008.
[12] S. Flohrer, R. Schäfer, J. McCord, S. Roth, L. Schultz, F. Fiorillo, W. Günther, G. Herzer, Magnetization loss and domain refinement in nanocrystalline tape wound cores, Acta Mater. 54 (2006) 4693–4698. https://doi.org/10.1016/j.actamat.2006.03.011.
[13] G.J. González, N. Murillo, J.M. Blanco, J.M. González, T. Kulik, Stress annealing in Fe73.5Cu1Ta3Si13.5B9 amorphous alloy: induced Magnetic anisotropy and variation of the magnetostriction constant, J. Appl. Phys. 76 (1994) 1131. https://doi.org/10.1063/1.357834.
[14] F. Alves, F. Simon, S.N. Kane, F. Mazaleyrat, T. Waeckerle, T. Save, A. Gupta, Influence of rapid stress annealing on magnetic and structural properties of nanocrystalline Fe74.5Cu1Nb3Si15.5B6 alloy, J. Magn. Magn. Mater. 294 (2005) e141–e144. https://doi.org/10.1016/j.jmmm.2005.03.071.
[15] G. Herzer, V. Budinsky, C. Polak, Magnetic properties of FeCuNbSiB nanocrystallized by flash annealing under high tensile stress, Phys. Status Solidi B 248 (2011) 2382–2388. https://doi.org/10.1002/pssb.201147088.
[16] H.R. Lashgari, J.M. Cadogan, D. Chu, S. Li, The effect of heat treatment and cyclic loading on nanoindentation behavior of FeSiB amorphous alloy, Mater. Des. 92 (2016) 919–931. https://doi.org/10.1016/j.matdes.2015.12.136.
[17] J.Z. Jiang, Anomalous grain growth in nanocrystalline Fe73.5Cu1Nb3Si13.5B9 alloys, Nanostruct. Mater. 9 (1997) 245–248. https://doi.org/10.1016/S0965-9773(97)90064-7.
[18] A. Hubert, R. Schäfer, Magnetic Domains, third ed., vol. 446, Springer Berlin Heidelberg, New York, 1998, p. 547.
[19] R. Schäfer, N. Mattern, G. Herzer, Stripe domains on amorphous ribbons, IEEE Trans. Magn. 32 (1996) 4809–4811. https://doi.org/10.1109/20.539159.
[20] K. Narita, J. Yamasaki, H. Fukunaga, Measurement of saturation magnetostriction of a thin amorphous ribbon by means of small-angle magnetization rotation, IEEE Trans. Magn. 16 (1980) 435–439. https://doi.org/10.1109/TMAG.1980.1060610.
[21] J. Torrens-Serra, I. Peral, J. Rodriguez-Viejo, M.T. Clavaguera-Mora, Microstructure evolution and grain size distribution in nanocrystalline FeNbBCu from synchrotron XRD and TEM analysis, J. Non-Cryst. Solids 358 (1) (2012) 107–113. https://doi.org/10.1016/j.jnoncrysol.2011.09.003.
[22] T. Gunes, R. Schäfer, N. Derebasi, Quantitative analysis of magnetic field distribution around circular non-magnetic region in grain-oriented Fe-3% Si steel, IEEE Trans. Magn. 54 (2018) 1–8. https://doi.org/10.1109/TMAG.2017.2755583.
[23] R. Schäfer, Nanoscale Magnetic Materials and Applications, first ed., Springer Dordrecht Heidelberg London, New York, 2009, pp. 277–283.
[24] J. Zhou, L. Meng, F. Yang, G. Ma, L. Chen, Effect of heat treatment on dynamic magnetic properties and microstructures of Fe73.5Cu1Nb3Si13.5B9 nanocrystalline alloy, J. Mater. Sci. Mater. Electron. 28 (2017) 6829–6836. https://doi.org/10.1007/s10854-017-6381-0.
[25] G. Herzer, NATO Sci. II Math. Phys. Chem. 184 (2005) 15.
[26] S. Flohrer, R. Schäfer, G. Herzer, Magnetic microstructures of nanocrystalline FeCuNbSiB soft magnets, J. Non-Cryst. Solids 354 (2008) 5097–5100. https://doi.org/10.1016/j.jnoncrysol.2008.07.034.
[27] C. Huang, X. Peng, B. Yang, S. Weng, Y. Zhao, T. Fu, Grain size dependence of tensile properties in nanocrystalline diamond, Comput. Mater. Sci. 157 (2019) 67–74. https://doi.org/10.1016/j.commatsci.2018.10.027.
[28] C. Huang, X. Peng, B. Yang, X. Chen, Q. Li, D. Yin, T. Fu, Effects of strain rate and annealing temperature on tensile properties of nanocrystalline diamond, Carbon 136 (2018) 320–328. https://doi.org/10.1016/j.carbon.2018.04.052.
[29] T.-Y. Kim, J.E. Dolbow, E. Fried, Numerical study of the grain-size dependent Young's modulus and Poisson's ratio of bulk nanocrystalline materials, Int. J. Solids Struct. 49 (2012) 3942–3952. https://doi.org/10.1016/j.ijsolstr.2012.08.023.